Detection of incomplete ellipse in images with strong noise by iterative randomized Hough transform (IRHT)

Wei Lu, Jinglu Tan*

Department of Biological Engineering, University of Missouri, Columbia, MO 65211, USA

Abstract

An iterative randomized Hough transform (IRHT) is developed for detection of incomplete ellipses in images with strong noise. The IRHT iteratively applies the randomized Hough transform (RHT) to a region of interest in the image space. The region of interest is determined from the latest estimation of ellipse parameters. The IRHT "zooms in" on the target curve by iterative parameter adjustments and reciprocating use of the image and parameter spaces. During the iteration process, noise pixels are gradually excluded from the region of interest, and the estimation becomes progressively close to the target. The IRHT retains the advantages of RHT of high parameter resolution, computational simplicity and small storage while overcoming the noise susceptibility of RHT. Indivisible, multiple instances of ellipse can be sequentially detected. The IRHT was first tested for ellipse detection with synthesized images. It was then applied to fetal head detection in medical ultrasound images. The results demonstrate that the IRHT is a robust and efficient ellipse detection method for real-world applications.
© 2007 Elsevier Ltd. All rights reserved.

Keywords: Curve detection; Randomized Hough transform; Hough transform; Image processing; Ellipse; Ultrasound; Fetal head

1. Introduction

Detecting curves of specific shapes is an important task in computer vision. Least-squares-based curve-fitting has been a commonly used category of methods employed for this purpose. A major disadvantage of these methods is that they are susceptible to the influences of outlier, noise and extraneous pixels [1–3]. Reduction of outliers heavily relies on data preprocessing based on curve symmetry [1] and heuristics of curve shape [2]. The preprocessing, however, may become ineffective when moderate noise, curve discontinuities, or image artifacts present [1–3]. Estimation methods with improved robustness have been proposed to reduce the effects of outliers [4]. For example, squared residuals are replaced by the median of squared residuals in the least median of squares (LMS) method, or by a function of the residuals with slower growth than squares in the *M*-estimators method [4]. These methods, however, usually require the fraction of outliers to be less than 50% of the total number of points.

The standard Hough transform (HT) and its variations seek an estimation of parameters by clustering in the parameter space [1,5]. The HT is relatively robust against outliers and curve discontinuities. It has been widely used for the detection of curves, especially lines [5–8]. Extending the HT to higher-dimensional curves, however, generates a high-dimensional parameter space, which causes many difficulties for reliable detection [6,9]. Geometric properties such as symmetry have been used to decompose a high-dimensional parameter space into two lower-dimensional parameter spaces, which separates the detection into two stages: locating the curve center and determining the remaining parameters [10–14]. This approach fails if the image does not have the required geometric properties [11,12]. Another approach uses the gradient of edges to reduce the dimension of the parameter space [5,15]. It is, however, hard to obtain the gradient accurately in noisy images [12]. Both approaches are not readily applicable to incomplete curves in images with strong noise because incomplete curves do not fully retain their geometric properties and the gradient of edges is often corrupted by noise. These limitations of the standard HT techniques are partially due to the fact that a pixel is counted for all instances of the shape on which the pixel may lie [9,16].

---

* Corresponding author. Tel.: +1 573 882 7778; fax: +1 573 884 5650.
  E-mail address: TanJ@missouri.edu (J. Tan).

This generates a great deal of redundant and misleading evidence in the parameter space.

To overcome some limitations of the standard HT, a new family of Hough transforms has been proposed to sample image data in various ways. Members of this family include the combinatorial Hough transform (CHT) [17], the randomized Hough transform (RHT) [16,18], the probabilistic Hough transform (PHT) [19], and the dynamic generalized Hough transform (DGHT) [9]. The PHT randomly selects a small subset of pixels for further processing. The other transforms share the following fundamental idea and are hereinafter referred to as RHTs. For an n-dimensional curve, a sample of n randomly picked pixels is used to solve for the n parameters of the curve. The count for the solution (an instance of the model) is increased by one in the parameter space. This process is repeated until enough solutions are accumulated so that there is a meaningful count distribution in the parameter space. The peak count and its coordinates in the parameter space correspond, respectively, to the most prominent curve instance in the image space and curve parameters. This random sampling (of n points) and convergent mapping (of n points to one solution) are the key mechanisms of RHTs, accounting for their favorable properties of small storage, high speed, good accuracy and reduced effects of correlated noise [16].

The random sample consensus (RANSAC) algorithm proposed by Fischler and Bolles [20] shared the two key mechanisms of RHTs. The RANSAC also randomly samples n data points to obtain an instance of the model. Instead of accumulating the counts as in the RHTs, the RANSAC examines the number of the consensus points that are within some error tolerance of the instance. If this number is greater than some threshold, a model is solved with the consensus points; otherwise, another set of n points is sampled and the process is repeated.

When noise is strong, both RHTs and RANSAC may fail as noise can corrupt the curve-related peaks in the parameter space, or can generate a larger consensus set for a false model instance. An improved method named the iterative randomized Hough transform (IRHT) is proposed in this paper for detection of incomplete ellipses under strong noise conditions. The IRHT iteratively applies a randomized Hough transform to a region of interest in the image space. The region of interest is updated based on the latest estimates of parameters. Two key features of the IRHT are: iterative parameter adjustment and reciprocating use of the image space and parameter space.

The IRHT was first tested for ellipse detection with synthesized images. It was then applied to fetal head detection in medical ultrasound images. Analysis of fetal head with ultrasound imaging is a daily routine for obstetricians, radiologists and sonographers. The image of a human fetal head is assumed to have an elliptical shape [21]. The biparietal diameter (BPD) and the head circumference (HC) are two important measurements for evaluating fetal growth [22], estimating gestational age [23–25], predicting fetal maturity [22] and weight [26], and diagnosing a wide range of obstetric problems [27]. The BPD is the distance from the outer margin of the proximal skull to the inner margin of the distal skull, and is usually measured as the distance between two manually marked endpoints. The HC is the circumference of the outer skull, and is manually measured by tracing the skull or fitting an ellipse to it with a mouse-like device [21]. An IRHT-based method was developed for automatic head detection as well as measurements of BPD and HC. The effectiveness of the IRHT-based method was demonstrated in this real-world application.

2. The iterative randomized Hough transform

2.1. Randomized Hough transform (RHT)

2.1.1. Brief description of the RHT transform

Let $\mathbf{z} = (x, y)$ represent the coordinates of a pixel in a binary image. Pixel refers to a foreground pixel with a binary value 1 throughout this paper. Assume that the curve to be detected can be modeled by $f(\mathbf{c}, \mathbf{z}) = 0$, where $\mathbf{c} = [\alpha_1, \ldots, \alpha_n]^t$ comprises n parameters. The RHT first draws a sample of n randomly picked pixels $\mathbf{z}_i = (x_i, y_i), i = 1, \ldots, n$, and then maps this sample into one point $\mathbf{c} \in R^n$ in the n-dimensional parameter space by solving a set of n equations $f(\mathbf{c}, \mathbf{z}_i) = 0$. If $\mathbf{c}$ defines a "valid" model instance (defined in Section 2.2.1 for ellipse), the count at $\mathbf{c}$ is increased by one in the parameter space and this count is stored in some types of discrete storage (accumulators). This process is repeated until a predetermined number of valid samples (K) are processed or a stopping criterion is met. A count peak in the accumulators corresponds to a prominent incidence of the curve in the image while the coordinates of the peak give an estimate of the parameters. For example, for an ellipse (where $n = 5$) the following stable and parametrically linear model can be used [9,28]:

$$x^2 + y^2 - U(x^2 - y^2) - V2xy - Rx - Sy - T = 0. \qquad (1)$$

The five parameters, $[U, V, R, S, T]^t$, can be converted into the commonly used ellipse parameters of $\mathbf{c} = [x_0, y_0, a, b, \phi]^t$, where (x_0, y_0) are the center coordinates, a and b are the major and minor semi-axes, and ϕ is the angle of rotation [9,28]. To save storage space and to simplify computation, five one-dimensional (1-D) accumulators, each of which stores the counts for one parameter, may be used instead of a *five*-dimensional (5-D) accumulator. The five peaks in the five accumulators give five estimated parameters of the ellipse [9].

2.1.2. Noise interference problem

It has been noted that interferences may result from noise for HT and RHTs [9,16,18,29]. Strong noise may completely corrupt the peaks in the parameter space, leading to detection failures. Each variation of the RHTs addresses this problem via a different mechanism, but none solve it satisfactorily. Ben-Tzvi and Sandler [17] did CHT on overlapping sub-images, and then merged the results. This approach was found useful but only applicable for line detection. Xu et al. [18] and Xu and Oja [16] performed curve detection in a stepwise manner. When a predetermined count threshold was reached, sampling was terminated and the detected curve was removed; then this process was repeated for the next curve. Significant misidentifications may occur even in the early steps under appreciable noise. Gerig [30] used a back-mapping technique to associate
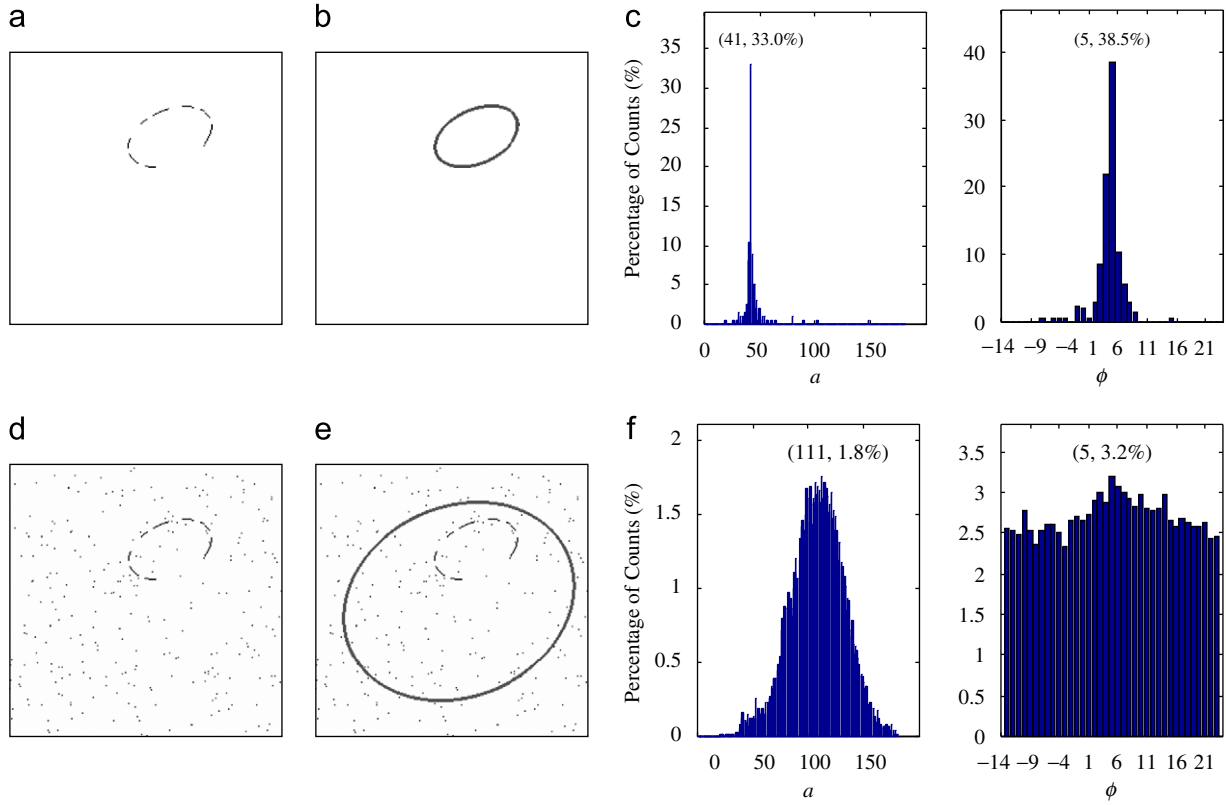
Fig. 1. Application of RHT to two synthesized images. (a) An incomplete (91 out of 188 pixels) ellipse defined by $[x_0, y_0, a, b, \phi]^t = [150, 79, 41, 25, 23°]^t$. (b) Detected ellipse by RHT for (a) with 200 samples. (c) Parameter histograms for (b). (d) Ellipse in (a) plus impulse noise (273 noise pixels). (e) Detected ellipse by RHT for (d) with 20,000 samples. (f) Parameter histograms for (e).

the cell with the highest vote in the parameter space to the corresponding feature points in the image space and to eliminate other cells on each hypersurface. Again, with strong noise, the cell with the highest vote may not correspond to the curve to be detected.

Leavers [9] first identified the connected points (left or top most pixels of horizontal or vertical line segments), and then used *a priori* curve size information to divide an image into subimages, each of which could include only one curve instance. For incomplete curves with nonuniform noise, this approach may either fail to identify any connected points on the true curve or may mistakenly identify many connected points from irrelevant structures. Moreover, the size range is not always known.

To illustrate the noise interference problem, the RHT described in Section 2.1.1 was applied to two synthesized images (Fig. 1). All synthesized images used in this paper were binary images of size 256×256 pixels. Fig. 1(a) contains an ellipse with discontinuities. Fig. 1(d) contains the same ellipse plus strong random impulse noise (or "salt and pepper" noise). Random noise was used because random sampling is independent of pixel connectivity and thus random noise represents a general noise for RHTs. The RHT-detected ellipse is shown as thick gray lines in Figs. 1(b) and (e). In the parameter space, parameters x_0, y_0, a and b were recorded in integers (pixels). Parameter ϕ, in the range of 0° to 180°, was quantized into

36 bins of 5° each. Since the count histograms of the first four parameters were similar, only the histograms of a and ϕ are shown (Figs. 1(c) and (f)). When there was no noise, with a small sample size $K = 200$, the true ellipse was accurately detected (Fig. 1(b)). Each histogram had a tight distribution around a sharp peak whose location gave the estimated parameter (Fig. 1(c)). On the other hand, when there was noise, even with a very large sample size $K = 20,000$, the RHT failed to detect the ellipse (Fig. 1(e)). The peaks in the histograms were not sharp and their locations did not corresponded to the true parameter values (Fig. 1(f)). The detection failure was due to noise interference. The noise pixels corrupted the true peaks in the histograms [9,16,18,29]. Similar results were obtained with a joint 5-D accumulator array instead of the five 1-D accumulators. Notice that the RANSAC would give similar results to Fig. 1(e) since the largest consensus set is those points around the false ellipse shown.

2.2. Iterative randomized Hough transform (IRHT)

2.2.1. The iterative randomized Hough transform algorithm

Noise interference persists because RHTs draw samples with equal probability from all pixels. If the probability of drawing pixels from the target curve is increased, the influence of the curve will be increased and noise interference reduced.
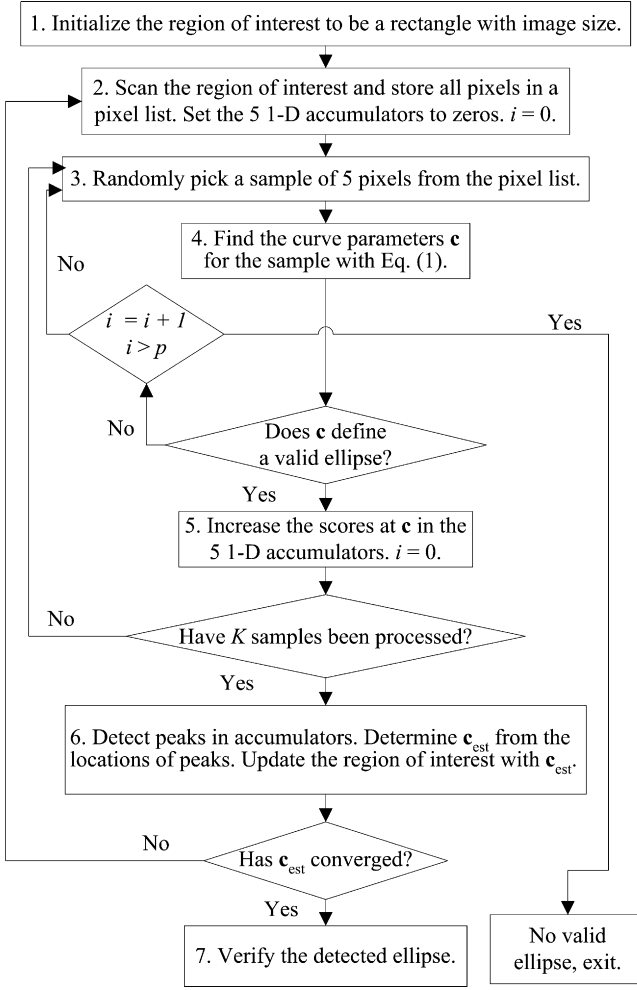
Fig. 2. Flow diagram of the iterative randomized Hough transform for ellipse detection.

Note that many noise pixels lie outside the estimated ellipse in Fig. 1(e). If the RHT is applied to pixels within this estimated ellipse rather than all pixels in the image, an improved estimation would result since the probability of drawing pixels from the curve is increased. It is expected that as the RHT is iteratively applied within each newly estimated ellipse, noise pixels are gradually excluded and better estimations obtained. This led to the development of the iterative RHT.

A flow diagram of the IRHT algorithm for ellipse detection ($n = 5$) is shown in Fig. 2. In step 1, a region of interest, defined as the region in which the target ellipse is most likely to lie, is initialized with the entire image. In step 2, the region of interest is scanned and all foreground pixels stored in a pixel list. The five 1-D accumulators are initialized with zeros. In steps 3–4, a sample of five pixels is randomly picked from the pixel list, and a parameter solution $c([x_0, y_0, a, b, \phi]^t)$ is found for this sample with Eq. (1). To ensure that c represents a valid ellipse, the following conditions need to be met: x_0, y_0, a, and b are positive, x_0 and y_0 are not larger than the image width and height, respectively, and a and b are not longer than one half of the diagonal length of the image. If c is valid, the

corresponding counts for c are increased the five 1-D accumulators; otherwise, c is discarded and a new sample is drawn. This random sampling and count accumulation process (steps 3–5) is repeated until K valid samples are processed.

In the unlikely event that no valid c is found for a given poll of a large number (p) of samples, the program exits and reports failure of detection. The probability of failure (P_f) is smaller than the probability that the RHT fails to draw at least one sample from the true ellipse and the latter can be estimated by the approach taken in Ref. [31] as follows. Assume that p samples of five points are drawn randomly from an image with N_e points on an ideal ellipse and N_n noise points (total points $N = N_e + N_n$) and l samples have all five points on the ellipse, the curve detection failure probability is

$$P_f < P(l \leqslant 1) = \sum_{k=0}^{1} \binom{p}{k} \left[\left(\frac{N_e}{N} \right)^5 \right]^k \left[1 - \left(\frac{N_e}{N} \right)^5 \right]^{p-k}. \quad (2)$$

When the ellipse is not ideal and only αN_e ($0 < \alpha < 1$) points are sufficiently close to the ellipse,

$$P_f < \sum_{k=0}^{1} \binom{p}{k} \left[\left(\frac{\alpha N_e}{N} \right)^5 \right]^k \left[1 - \left(\frac{\alpha N_e}{N} \right)^5 \right]^{p-k}. \quad (3)$$

Detection failure occurs when the detection task is a difficult one; i.e., $\alpha N_e / N \ll 1$. Then, the RHT failure probability depends on $l_e = p(\alpha N_e / N)^5$, the expected value of l. When the poll size p is too small in the sense that $l_e \ll 1$, the probability of RHT failure is close to 1. If p is sufficiently large so that $l_e \gg 1$, which should be the normal operating condition, the probability of RHT failure is

$$P_f < P(l \leqslant 1) \approx \left[1 - \left(\frac{\alpha N_e}{N} \right)^5 \right]^{p-1} p \left(\frac{\alpha N_e}{N} \right)^5. \quad (4)$$

Eq. (4) indicates that the failure probability decreases with increasing poll size (p). In other words, the likelihood of detection failure can be controlled by using a sufficiently large poll size. For a given maximum failure probability, the necessary poll size can be estimated from the equation.

In step 6, a parameter estimate, c_{est}, is determined from the locations of the count peaks in the 1-D accumulators. c_{est} corresponds to the most likely ellipse estimated from the current region of interest. Though this ellipse could be used as a new region of interest for the next iteration, a slightly larger region is used instead to compensate for uncertainties in the estimated parameters (see Section 2.2.2). If the change in c_{est} from the previous iteration is small (in this work: less than 2.5° in ϕ; less than two pixels in each of x_0, y_0, a, and b; and less than six pixels total in x_0, y_0, a, and b), the algorithm is considered to have converged. Otherwise, the RHT process (steps 2–6) is repeated in the new region of interest. Finally, the detected ellipse may be verified based on the specific application. The number of samples per iteration (K) should be large enough so that the parameter histograms have sufficient entries. The choice of K, however, does not need to be precise since the algorithm iteratively adjusts the results.
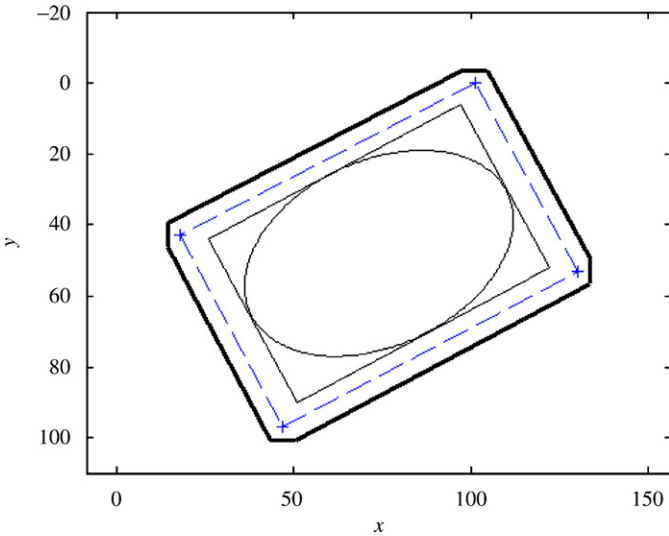
Fig. 3. Design of region of interest for ellipse.

The IRHT does not require *a priori* information about the ellipse (size range, angle of rotation, etc.). When such information is available, however, it can be easily incorporated into the algorithm for improved efficiency. For example, if the eccentricity ($e = b/a$) of the true ellipse is known to be equal to or larger than e_1, only parameter solutions with $e \geqslant e_1$ will be considered as valid instances. Constraints like this can significantly improve the IRHT performance as shown later.

2.2.2. Region of interest design for ellipse

The region of interest is an area that contains the target ellipse. The design of a region of interest is an important part of the IRHT. Although a different curve (e.g. ellipse, circle, line) may require a different region of interest, the design principles would apply.

If an image contains a prominent ellipse, the distribution of the computed parameter values would most likely show a peak in the parameter space. A joint confidence region of the estimated parameters is an ellipsoid centered at the peak in the 5-D parameter space [32]. This confidence region corresponds to a family of ellipses, which form a zone of irregular shape in the image space. For a given confidence level, this zone would theoretically be the logical choice of region of interest. Practically, however, accurate determination of this zone is computationally involved and may not prove fruitful. Furthermore, it requires the use of a 5-D parameter space, which could cause many difficulties for reliable curve detection [5,9]. In this work, an empirical method was used to find an approximation of the zone in the image space.

Suppose that RHT produces a parameter estimation of $\mathbf{c} = [x_0, y_0, a, b, \phi]^t$, with a standard error vector of $\sigma_c = [\sigma_x, \sigma_y, \sigma_a, \sigma_b, \sigma_\phi]^t$. Let $\Delta_{\mathbf{c}} = [\Delta_x, \Delta_y, \Delta_a, \Delta_b, \Delta_\phi]^t$, which is related to $\boldsymbol{\sigma}_c$, denote a desired set of enlargements of ellipse $\mathbf{c}$ to form a new region of interest. Fig. 3 illustrates a procedure to determine the region of interest for an ellipse with $0^\circ \leqslant \phi \leqslant 90^\circ$. The ellipse is first stretched by $2\Delta_a$ in the direction of major axis and by $2\Delta_b$ in the direction of minor

axis. The circumscribing rectangle of the stretched ellipse is displayed in dashed lines with its four vertices marked with '+'. The rectangle is then translated by $-\Delta_x$ or Δ_x in the x direction and by $-\Delta_y$ or Δ_y in the y direction. This creates an octagon (thick solid lines in Fig. 3), which can be used as a region of interest for the ellipse. The uncertainty in ϕ is not used ($\Delta_\phi = 0$) for two major reasons. First, possible ellipses inside the octagon already have a wide range of variation in ϕ. Second, with strong noise in the image, the estimated ϕ is neither accurate nor precise for the first several iterations. For an ellipse with $90^\circ < \phi \leqslant 180^\circ$, a similar approach can be used to obtain its region of interest. It was found that under strong noise conditions, the detection results were sensitive to the choice of $\Delta_{\mathbf{c}}$. The region of interest may not exclude enough noise pixels if $\Delta_{\mathbf{c}}$ is too large and it may not include a large enough part of the ellipse if $\Delta_{\mathbf{c}}$ is too small. For relatively low noise, however, the detection results were insensitive to the choice of $\Delta_{\mathbf{c}}$. In this study, $\Delta_{\mathbf{c}}$ was experimentally determined as $[\Delta_x, \Delta_y, \Delta_a, \Delta_b, \Delta_\phi]^t = [0.5\sigma_x, 0.5\sigma_y, 0.5\sigma_a, 0.5\sigma_b, 0]^t$. For a univariate normal distribution, an interval of ± 0.5 standard deviation corresponds to a 38% confidence interval. These seemingly small coefficients (0.5 and 0) are actually reasonable choices for two major reasons. First, a simultaneous confidence region based on the five 1-D marginal distributions is larger than the 5-D joint confidence region for the same coefficient values. Second, with a prominent ellipse in an image, the parameter count distributions are much tighter than the normal distribution. The choice of $\Delta_{\mathbf{c}}$ was found good for various conditions tested.

3. Results

3.1. Test of IRHT with synthesized images

Fig. 4 shows results of IRHT application to the image in Fig. 1(d). In this example, the IRHT converged after six iterations. The results of the first, third, and sixth iterations are shown. The region of interest is inside the octagon shown in gray lines. The resulting ellipse was superimposed on the image after the IRHT converged (Fig. 4(c)). Fig. 4 demonstrates that the IRHT progressively improved the estimations and converged to the target ellipse. During the iteration process, noise pixels were gradually excluded while the target ellipse was kept inside the region of interest. The parameter histograms became narrower and the peaks became sharper, implying more precise estimations. For this example, the five parameter estimates were exactly those of the true ellipse (Fig. 4(c)). The shapes of the histograms in Fig. 4(c) are similar to those in Fig. 1(c), which result from an image without noise. This suggests that the IRHT gradually reduced and eventually eliminated the interference of noise.

Fig. 5 shows detection of a blurred and incomplete ellipse in a background of random impulse noise. The locations of the ellipse pixels in Fig. 4(a) were further corrupted by a Gaussian noise with a zero mean and standard deviation (σ_g) of 2 in both the x and y directions (Fig. 5(a)). Nearly all the ellipse pixels became disconnected and no solid ellipse segments were
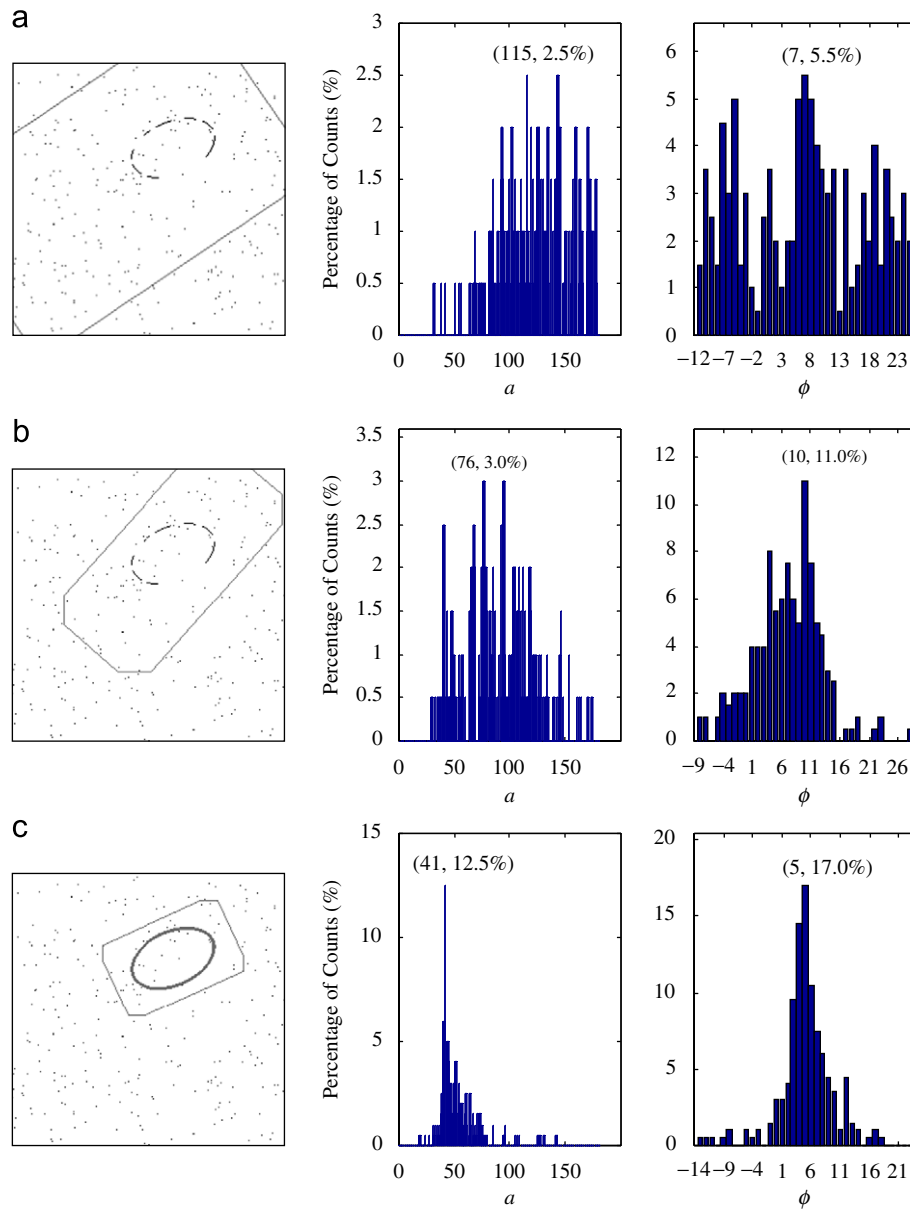
Fig. 4. Application of IRHT to the image in Fig. 1(d). (a) After the first iteration the estimation is far from the target and the histograms are wide. (b) After the third iteration the estimation becomes closer to the target and the histograms are narrower; local peaks around the true parameters become visible. (c) After the sixth iteration the IRHT converged to the target; global peaks are sharp at true parameters.
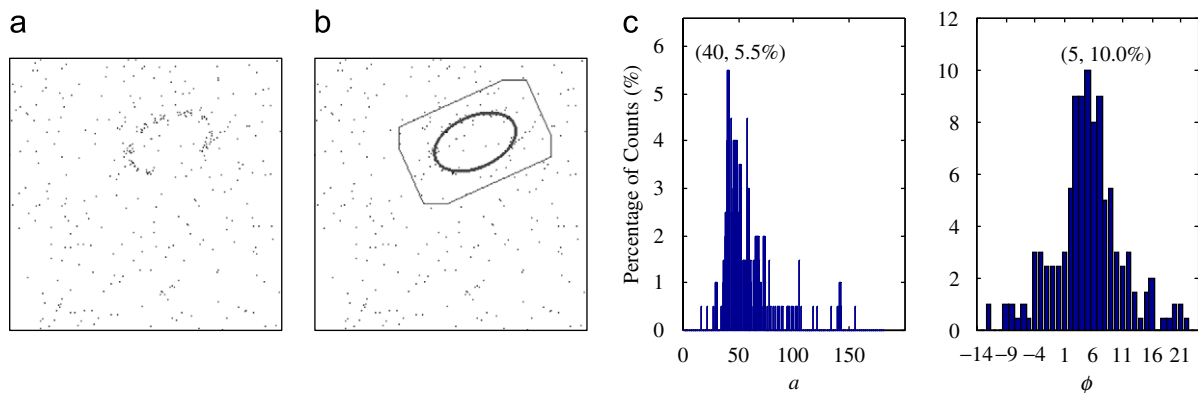

Fig. 5. Application of IRHT in detecting a blurred ellipse in an image with impulse noise. (a) An incomplete, Gaussian noise-corrupted ellipse (94 pixels) in a background of 282 impulse noise pixels. (b) The result of the IRHT for (a). (c) The final histograms of IRHT.

Table 1
IRHT performance on ellipse images with different noise types and levels

	$N_e : N_n = 91 : 273$	$N_e : N_n = 91 : 546$	$N_e : N_n = 90 : 270 \ \sigma_g = 1$	$N_e : N_n = 94 : 282 \ \sigma_g = 2$	$N_e : N_n = 94 : 282 \ \sigma_g = 2; \ e \geqslant 0.5$
Convergence rate	100%	100%	100%	87%	100%
Average iteration	8	29	19	31	13
$\varepsilon_d (\sigma_d)$	0.04 (0.20)	0.36 (0.72)	0.75 (0.71)	1.85 (4.18)	0.73 (0.74)
$\varepsilon_a (\sigma_a)$	0.00 (0.00)	0.41 (2.00)	0.54 (0.70)	0.78 (0.77)	0.35 (0.48)
$\varepsilon_b (\sigma_b)$	0.08 (0.27)	0.56 (0.88)	1.29 (1.23)	2.44 (1.81)	1.25 (1.59)
$\varepsilon_\phi (\sigma_\phi)$	1.00° (0.00°)	1.46° (1.60°)	1.89° (1.82°)	2.91° (2.88°)	1.24° (0.82°)

N_e, number of pixels from ellipse;
N_n, number of impulse noise pixels.

visible. Even with these severe disturbances, the IRHT estimation closely agreed with the true ellipse (Fig. 5(b)). The parameter histograms in Fig. 5(c) spread more than those in Fig. 4(c), but the peaks are still well defined. The noise led to some degradation in the estimation accuracy, which was also reported by Fitzgibbon et al. [3].

The IRHT was further tested with different combinations of noise types and levels in the incomplete-ellipse images (Table 1). For each combination, 100 images were used. The convergence rate was the percentage of images for which the algorithm converged within 100 iterations. The average iteration was the average number of iterations for the IRHT to converge. The error (ε) and the standard error (σ) were, respectively, the mean absolute difference between the estimated and the true parameter (shown by the subscripts) values, and the standard error of the estimated parameters. For the error calculations, distance, d, between the estimated and the true center locations was used instead of the differences in center coordinates (x_0 and y_0). For the first three combinations, the IRHT converged for all the 300 images. Almost all errors for d, a and b were less than 1 pixel, and all errors for ϕ were less than 2°. Moreover, all standard errors were less than 2 pixels or degrees. For the fourth combination involving both severe blurring (corruption of curve pixel locations by a Gaussian noise of zero mean and $\sigma_g = 2$) and strong random impulse noise, the IRHT converged for 87 of the 100 images. The errors for d, a and b were less than 2.5 pixels and the error for ϕ was less than 3°. The degradations in performance obviously resulted from the severe blurring. When a constraint $e \geqslant 0.5$ was used in the fifth case, however, the results were much improved. The convergence rate increased to 100% and the average number of iterations dropped from 31 to 13. Additionally, all estimation errors and almost all standard errors were significantly reduced. Using this constraint in the same way in the RHT, however, yielded little improvement.

3.2. Execution time and memory space usage

Since the IRHT in this study used n 1-D accumulators, peak detection was simple. Also because the IRHT iteratively adjusted the estimation, the number of samples (K) needed for each iteration was small compared with other RHT algorithms. Throughout this study, K was chosen to be 200. The average number of iterations (N_{iter}) needed for images with moderate noise was usually small (Table 1) and thus the total sample

size ($K \times N_{iter}$) was usually not large. Suppose that M is the greater of the image width and height, the total number of foreground pixels N is usually much smaller than M^2. The memory requirement of the IRHT is $\sum_{i=1}^{n} N_{ai} + N$, where N_{ai} is the accumulator size for the ith parameter and is of the order of $O(M)$. $\sum_{i=1}^{n} N_{ai} + N$ is therefore of the order of $O(M^2)$, and is much smaller than $\prod_{i=1}^{n} N_{ai}$, which is of the order of $O(M^n)$ and is the storage required by the standard Hough transform. The IRHT therefore achieves improved efficiency in both execution time and memory space usage.

3.3. Head Identification in ultrasound fetal images by the IRHT

3.3.1. Segmentation and detection of the fetal head

Fig. 6(a) shows a typical ultrasound fetal head image acquired by a sonographer during routine pregnancy examinations. Bones (head skull and femur etc.) appear as bright objects. Often, there are other bright structures adjacent to the head skull, and moderate to large gaps exist between skull segments. The image intensity is not always consistent, even among images acquired under apparently the same conditions. Furthermore, various artifacts and noises are usually present in an ultrasound image. As a result, thresholding or iterative dilation was found ineffective for fetal head segmentation. In this study, a K-mean algorithm [33,34] was used to classify each pixel according to its intensity value into one of the three groups: bright object, gray object and background. Preprocessing and post-processing were also performed to reduce noise and to smooth the object boundaries. Details of the segmentation algorithm was described in Lu and Tan [35]. The skeletons of the bright objects, which provided simple and adequate representations of the skull segments, were extracted (Fig. 6(b)) and the skeleton image was used for head detection by the IRHT.

Large gaps, artifacts and moderate nonuniform noise are usually present in the original and the skeleton images. The skeleton pixels of skull segments would practically never be on one ellipse. These disturbances make the fetal detection a challenging task, for which the IRHT was found particularly suitable. Hadlock et al. [23] reported that the cephalic index (or the eccentricity e) of the human fetal head has a mean (μ_e) of 0.783 and a standard deviation (σ_e) of 0.044. This *a priori* knowledge was used to construct a constraint as $\mu_e - 3\sigma_e \leqslant e \leqslant \mu_e + 3\sigma_e$, or $0.651 \leqslant e \leqslant 0.915$. About 99.7% of fetal heads would have
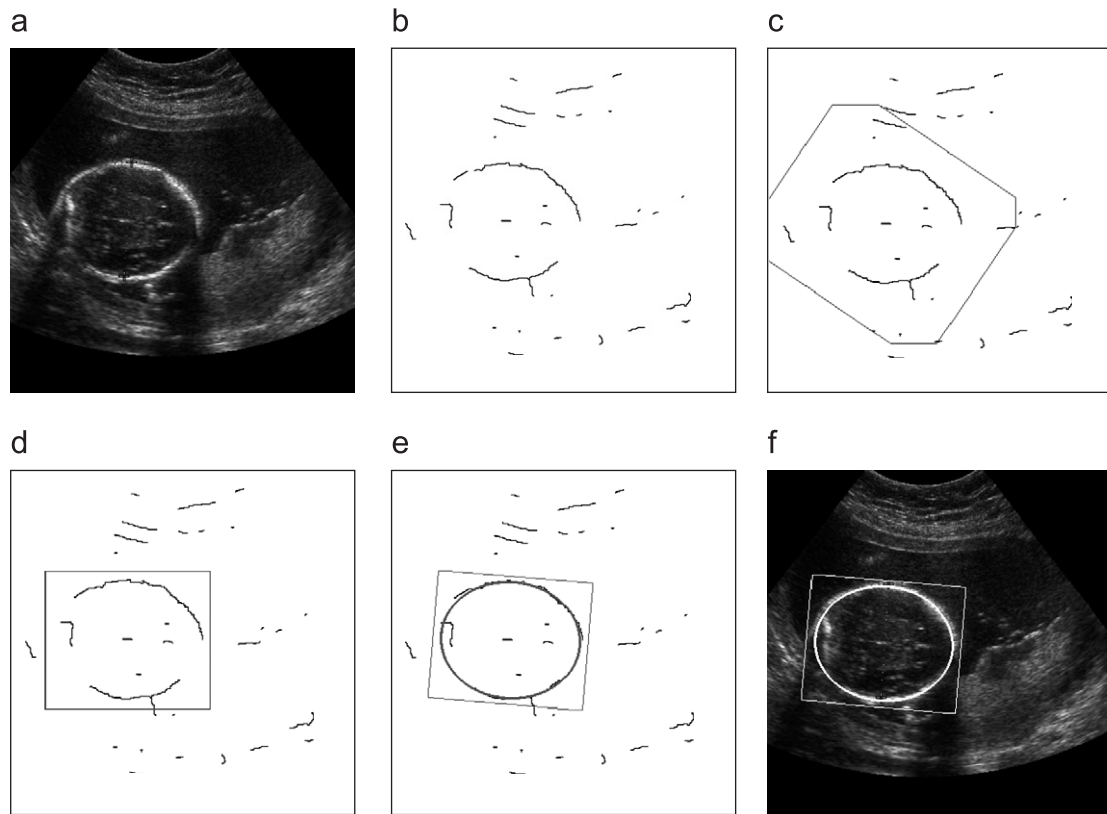
Fig. 6. Segmentation and detection of ultrasound fetal head. (a) A medical ultrasound fetal head image. (b) Skeletons of segmented bright objects used as input to the IRHT. (c) After the first iteration of the IRHT. (d) After the second iteration of the IRHT, the angle of rotation is still incorrect. (e) After the fifth iteration, the IRHT has converged and the detected ellipse is superimposed on the skeleton image. (f) The detected ellipse in (e) superimposed on (a).

an eccentricity in this range. All other algorithm settings were the same as those used for the tests with synthesized images. Figs. 6(c)–(f) show the results of the IRHT. The algorithm correctly converged to the head after five iterations. During the iteration process, the parameter histograms became narrower and the peaks sharper (not shown).

Eleven fetal head images were collected from patients during routine sonographic examination with a clinical ultrasound machine (ATL HDI 3000, Bothell, WA). The gestational age of the 11 fetuses was from 18 to 34 weeks. The IRHT converged for all images with an average number of five iterations and an average execution time of 1.1 s per image on a 933 MHz Pentium III PC. This time included times for reading and writing image, detecting and measuring the head, and outputting the results. The regular RHT failed to detect any of the head objects even after 20,000 samples were processed under the same eccentricity constraint.

3.3.2. BPD and HC measurements

The BPD and HC were measured from the resulting ellipse as described previously [36]. The averages of BPD and HC measured by two sonographers and six other trained personnel were used as the manual measurements. The averages of BPD and HC measured in eight runs of the IRHT were used as the automatic measurements. The mean absolute inter-observer and inter-run differences of the BPD and HC measurements

were calculated as the average of all absolute inter-observer and inter-run differences (%), respectively [36]. The inter-observer variation was 2.05% for BPD and 1.78% for HC, while the inter-run variations were smaller at 0.54% for BPD and 1.61% for HC for the 11 images. These statistics suggested that the automatic measurements were more consistent than the manual measurements for BPD and as consistent for HC. The improved consistency in BPD measurement was apparently because BPD was computed from a fitted head contour ellipse in the automatic method whereas it was measured from two subjectively selected points in the manual method.

The mean absolute differences and the correlations between the manual and automatic measurements of BPD and HC were calculated. The differences were 0.87 mm (1.66%) for BPD and 3.41 mm (1.74%) for HC. The correlation coefficients were 0.999 for BPD and 0.997 for HC. The differences were small compared with the published inter-observer variations of 2.0–7.0% as reported by Chalana et al. [37]. In the same paper, the heads in 33 of 35 ultrasound fetal head images were detected with a method based on the active contour model. The reported differences were 0.79 mm (1.41%) for BPD and 7.12 mm (2.99%) for HC, and the correlation coefficients were 0.999 for BPD and 0.994 for HC. The results for BPD in this research are highly comparable to the results reported in Ref. [37]. The results for HC in this work are better, which might be a result of smaller sample set used in this study. Compared

with the IRHT, the main disadvantages of the method used in Ref. [37] were that it required the user to input a point near the center of the head in each image, and that the active contour model was computationally complex. Compared with manual measurements, the automatic method was more consistent, indicating improved measurement objectivity.

4. Discussion

4.1. IRHT for multiple-ellipse detection and other curves

If it is possible to divide an image into sub-images, each of which includes only one ellipse, then every ellipse can be detected by applying the IRHT to every sub-image. Multiple-ellipse detection, however, is necessary when such a division is unfeasible. An example of this situation is shown in Fig. 7(a), which contains two overlapping ellipses E_1 and E_2 as well as strong background noise. The two ellipses cannot be divided into two sub-images. The IRHT was applied to the entire image, and E_1 was detected first (Fig. 7(b)) because there were more pixels on E_1 than on E_2. The pixels that were on or very close to E_1 were then removed from the original image, and the result is shown in Fig. 7(c). The IRHT was then applied to Fig. 7(c) leading to the detection of E_2 (Fig. 7(d)). By such a stepwise procedure, the most prominent ellipse is detected in each step because the IRHT is a probability-based algorithm. When multiple ellipses exist and no single ellipse is sufficiently prominent, the procedure based on 1-D accumulators may become ineffective since there may be multiple peaks in each accumulator and matching the peaks resulting from the same ellipse may become problematic. In this case, the IRHT may need to use an n-dimensional joint accumulator [16], and to detect local peaks instead of global peaks [29]. This is a limitation of the 1-D accumulators. They are simple but require prominence of an ellipse. While the prominence condition is fortunately valid for many applications, the use of an n-D joint accumulator for multiple-curve detection warrants further study.

The IRHT is presented in the context of ellipse detection, but it is a general algorithm that can be used for the detection of other parametric curves. The only differences lie in the curve model and in the design of the region of interest. For nonparametric curves, a generalization of the RHT for arbitrary shape detection is needed. One may refer to Ballard [15] for the generalization of the standard HT to arbitrary curves by using gradient direction information.

4.2. Using more than five pixels to estimate ellipse parameters

The potential benefits of using more than five pixels to estimate the five parameters of an ellipse were investigated. The expectation was that the filtering effect of more pixels would lead to more stable, and possibly better parameter estimates (particularly ϕ) than exactly five pixels. Suppose that m pixels ($m > n$) are picked for each sample instead of n pixels ($n = 5$). The linear system generated by Eq. (1) would have m equations for the five unknowns, and an optimal solution can be obtained by using the least-squares method. Several values for m were tested. For ellipses without noise, the histograms were narrower than those obtained with five pixels because the optimal solution filtered out some effects of the inexact pixel locations. For ellipses in an image with strong noise, however, the estimated parameters were not more accurate than those obtained with five pixels. This was apparently due to noise interference. Using more pixels for an optimal solution could potentially reduce the overall variability of the parameter estimates, but it would also reduce the sharpness of the histogram peaks because the chance to draw all pixels in a sample from the target ellipse decreases with increasing number of pixels in a sample since $(\alpha N_e/N)^m < (\alpha N_e/N)^5$, $m > 5$. This increases the probability of detection failure for a given poll size p as shown by Eq. (4). Conversely, to achieve the same failure rate, the required poll size p will be $(N/\alpha N_e)^{m-5}$ times of that for five pixels. Since a reduction in estimate variability does not necessarily lead to improved estimation accuracy but a sharper peak resulting from the target curve will, using more than five pixels does not seem to bring benefits in general.

4.3. Effect of image shape

For an image of only random impulse noise, the outcome of RHT depends on the size and shape of the image. For example, for a square image of only random impulse noise, the RHT identifies an ellipse located at the image center with ϕ in the diagonal direction (45° or 135°). This fact could be used to improve the estimation for images with moderate random impulse noise. Figs. 8(a) and (b) show the resulting ellipse and
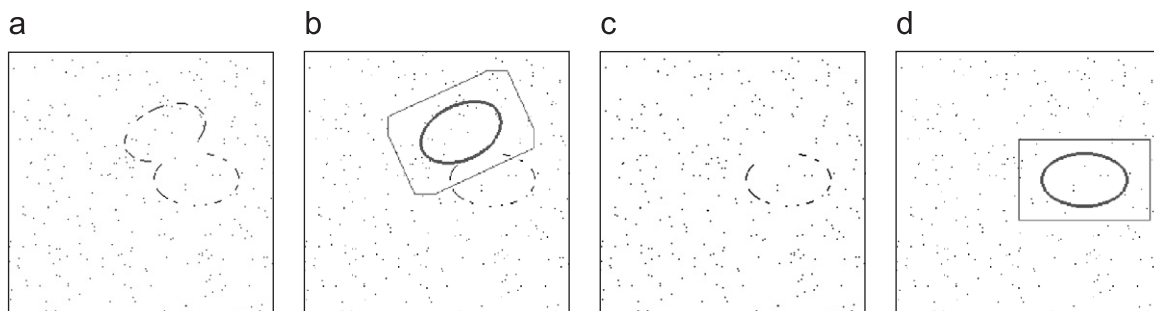

Fig. 7. An example application of IRHT for multiple-instance detection. (a) An image of two ellipses E_1, E_2. (91 pixels for E_1, 68 pixels for E_2, and 273 impulse noise pixels). (b) E_1 first detected. (c) After removal of E_1. (d) E_2 detected.
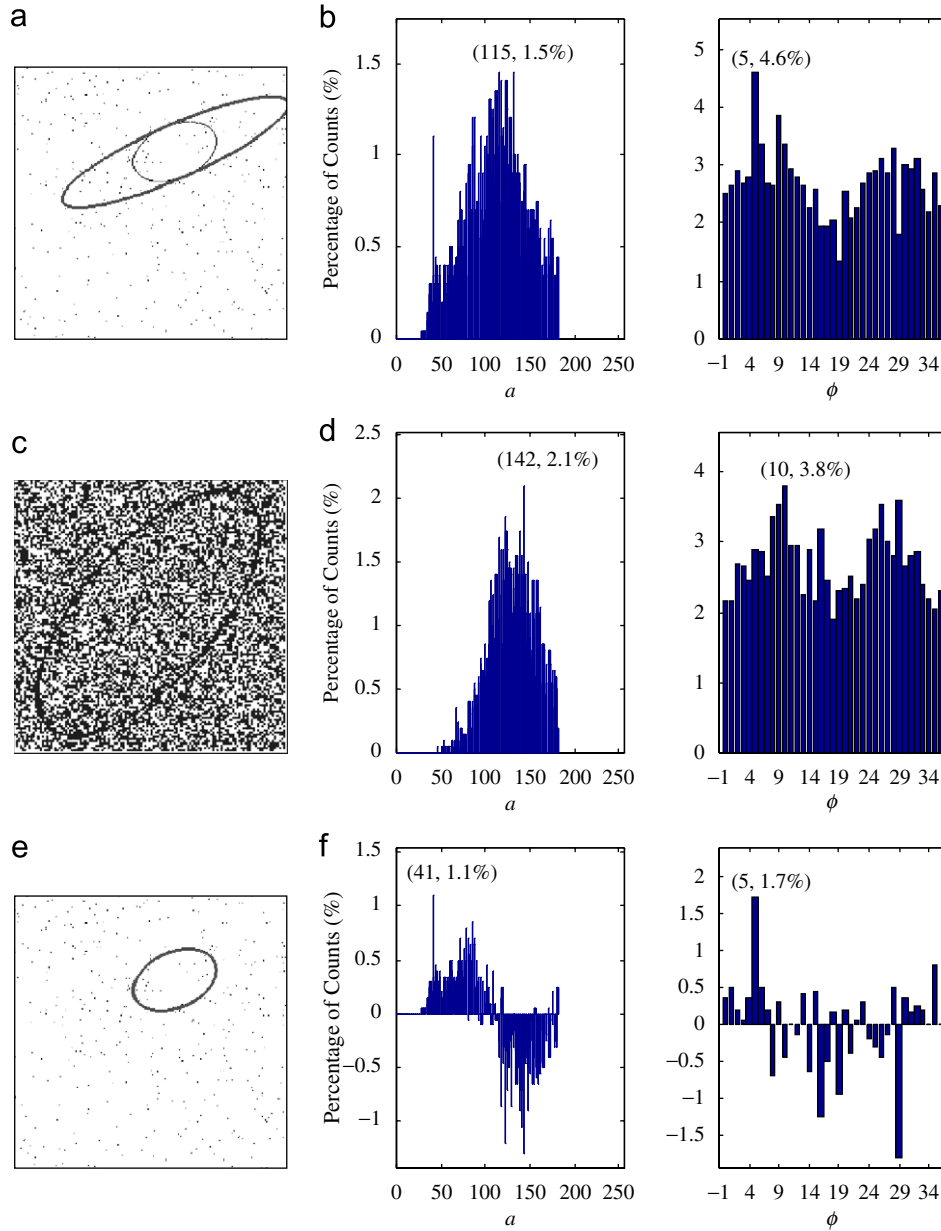
Fig. 8. Subtractive compensation for image shape effects. (a) A much longer ellipse identified by RHT for an ellipse of 188 pixels with 376 background noise pixels. (b) Histograms corresponding to (a). (c) Ellipse from RHT for an image of random noise. (d) Histograms corresponding to (c). (e) Ellipse detected after subtracting histograms in (d) from those in (b). (f) Histograms after the subtraction.

histograms of RHT for an image containing an ellipse and moderate impulse noise. As shown in Fig. 8(a), the RHT-estimated major semi-axis a was severely biased by the noise. Though the ellipse resulted in a local peak at the true value of a (41), the peak was lower than the global one, which resulted from the noise (Fig. 8(b)). Figs. 8(c) and (d) are the resulting ellipse and histograms of applying RHT to an image of only impulse noise. The ellipse is located at the image center and there are two peaks at the diagonal directions (45° and 135°) in the ϕ histogram. Fig. 8(f) shows the results of subtracting the histograms in Fig. 8(d) from those in Fig. 8(b). The subtraction cancels some contribution from the noise and allows the true peak of a to emerge while making the true peak of ϕ sharper.

The global peaks in Fig. 8(f) define the ellipse in Fig. 8(e), which is a much better estimation than the one in Fig. 8(a). This subtractive compensation can be used in the first iteration of the IRHT to expedite convergence.

4.4. Comparison of IRHT with other methods

Compared to other robust estimation methods such as LMS, M-estimators and RANSAC, the reciprocating use of the image and parameter spaces in the IRHT is novel and has shown effectiveness in outlier rejection. LMS and M-estimators assume that outliers constitute a minority ($< 50\%$) of the data. Using random sampling and converging mapping, the RANSAC is

similar to the RHT and both can deal with more than 50% outliers. The difference is that the RANSAC examines the number of consensus points for each model instance, while the RHT examines the peak count in the parameter space for all model instances. Both methods may fail in cases of strong outliers as shown in Fig. 1(e). The IRHT, however, succeeds in such cases by having a mechanism to exclude outliers progressively. The region of interest is narrowed and improved through iteration, allowing the IRHT algorithm to focus on the target curve (Figs. 4–7). The focusing mechanism (region of interest) based on two reciprocating spaces is the main feature the IRHT.

5. Summary

An iterative randomized Hough transform is developed to overcome the limitations of existing methods for detection of incomplete ellipses in images with strong noise. The proposed IRHT retains the advantages of the randomized Hough transform with improved robustness and efficiency. The iterative parameter adjustments and the reciprocal use of the image and parameter spaces account for the advantages of the IRHT. The IRHT detects the most prominent instance of ellipse and works effectively for indivisible, multiple-instance detection. The IRHT has been developed for parametric curve detection, and extension to nonparametric curve detection is possible. As opposed to existing methods for head detection in ultrasound fetal images, the IRHT does not require user intervention or size range of the head. The differences between the IRHT-based automatic measurements and manual measurements were insignificant and the automatic method was more consistent. The results demonstrated that the IRHT is a robust and efficient ellipse detection method in real-world applications.

References

[1] W.-Y. Wu, M.-J.J. Wang, Elliptical object detection by using its geometric properties, Pattern Recogn. 26 (1993) 1499–1509.

[2] D. Zhu, S.T. Moore, T. Raphan, Robust pupil center detection using a curvature algorithm, Comput. Methods Programs Biomed. 59 (1999) 145–157.

[3] A. Fitzgibbon, M. Pilu, R.B. Fisher, Direct least square fitting of ellipses, IEEE Trans. Pattern Anal. Mach. Intell. 21 (1999) 476–480.

[4] Z. Zhang, Parameter estimation techniques: a tutorial with application to conic fitting, Image Vision Comput. 15 (1997) 59–76.

[5] J. Illingworth, J. Kittler, Survey of the Hough transform, CVGIP 44 (1988) 87–116.

[6] R. Duda, P. Hart, Use of the Hough transformation to detect lines and curves in pictures, Comm. ACM 15 (1972) 11–15.

[7] Y. Zhang, R. Webber, Windowing approach to detecting line segments using Hough transform, Pattern Recogn. 29 (1996) 255–265.

[8] A.L. Kesidis, N. Papamarkos, Window-based inverse Hough transform, Pattern Recogn. 33 (2000) 1105–1117.

[9] V.F. Leavers, The dynamic generalized Hough transform: its relationship to the probabilistic Hough transforms and an application to the concurrent detection of circles and ellipses, CVGIP: Image Understanding 56 (1992) 381–398.

[10] S. Tsuji, F. Matsumoto, Detection of ellipses by a modified Hough transformation, IEEE Trans. Comput. C-27 (1978) 777–781.

[11] H.K. Yuen, J. Illingworth, J. Kittler, Detecting partially occluded ellipses using the Hough transform, Image Vision Comput. 7 (1989) 31–37.

[12] C.-T. Ho, L.-H. Chen, High-speed algorithm for elliptical object detection, IEEE Trans. Image Process. 5 (1996) 547–550.

[13] P.S. Nair, A.T.J. Saunders, Hough transform based ellipse detection algorithm, Pattern Recogn. Lett. 17 (1996) 777–784.

[14] R.A. McLaughlin, Randomized Hough transform: improved ellipse detection with comparison, Pattern Recogn. Lett. 19 (1998) 299–305.

[15] D.H. Ballard, Generalizing the Hough transform to detect arbitrary shapes, Pattern Recogn. 13 (1981) 111–122.

[16] L. Xu, E. Oja, Randomized Hough transform (RHT): basic mechanisms, algorithms, and computational complexities, CVGIP: Image Understanding 57 (1993) 131–154.

[17] D. Ben-Tzvi, M.B. Sandler, A combinatorial Hough transform, Pattern Recogn. Lett. 11 (1990) 167–174.

[18] L. Xu, E. Oja, P. Kultanen, A new curve detection method: randomized Hough transform (RHT), Pattern Recogn. Lett. 11 (1990) 331–338.

[19] N. Kiryati, Y. Eldar, A.M. Bruckstein, Probabilistic Hough transform, Pattern Recogn. Lett. 24 (1991) 303–316.

[20] M.A. Fischler, R.C. Bolles, Random sample consensus: a paradigm for modle fitting with applications to image analysis and automated cartography, Commun. ACM 24 (1981) 381–395.

[21] P. Athey, F. Hadlock, Ultrasound in Obstetrics and Gynecology, second ed., The C.V. Mosby Com., St. Louis, MO, 1985.

[22] F. Hadlock, Ultrasound evaluation of fetal growth, in: P. Callen (Ed.), Obstetrics and Gynecology, second ed., Saunders, Philadelphia, PA, 1988, pp. 129–142.

[23] F.P. Hadlock, R.L. Deter, R.J. Carpenter, S.K. Park, Estimating fetal age: effect of head shape on BPD, Am. J. Roentgenol. 137 (1981) 83–85.

[24] F.P. Hadlock, R.L. Deter, R.B. Harrist, S.K. Park, Estimating fetal age: computer-assisted analysis of multiple fetal growth parameters, Radiology 152 (1984) 497–501.

[25] F.P. Hadlock, R.L. Deter, R.B. Harrist, S.K. Park, Computer assisted analysis of fetal age in the third trimester using multiple fetal growth parameters, J. Clin. Ultrasound 11 (1983) 313–316.

[26] I. Gull, G. Fait, J. Har-Toov, M.J. Kupferminc, J.B. Lessing, A.J. Jaffa, I. Wolman, Prediction of fetal weight by ultrasound: the contribution of additional examiners, Ultrasound Obstet. Gynecol. 20 (2002) 57–60.

[27] J. William, S. Roya, Introduction to ultrasound, W.B. Saunders Company, PA, 1998.

[28] A.B. Forbes, Fitting an ellipse to data, National Physical Laboratory Report DITC 95/87, 1987.

[29] C.M. Brown, Inherent bias and noise in the Hough transform, IEEE Trans. Pattern Anal. Mach. Intell. 5 (1983) 493–505.

[30] G. Gerig, Linking image-space and accumulator-space: a new approach for object recognition, in: Proceedings First International Conference on Computer Vision, IEEE Computer Society and International Association for Pattern Recognition, London, 8–11 June, 1987, IEEE, New York, pp. 112–117.

[31] N. Kiryati, H. Kalviainen, S. Alaoutinen, Randomized or probabilistic Hough transform: unified performance evaluation, Pattern Recogn. Lett. 21 (2000) 1157–1164.

[32] R. Johnson, D. Wichern, Applied Multivariate Statistical Analysis, Prentice-Hall, Upper Saddle River, NJ, 1998.

[33] J.T. Tou, R.C. Gonzalez, Pattern Recognition Principles, Addison-Wesley, Reading, MA, 1974.

[34] R.O. Duda, P.E. Hart, D.G. Stork, Pattern Classification, secon ed., Wiley, New York, NY, 2001.

[35] W. Lu, J. Tan, Segmentation of ultrasound fetal images, in: Biological Quality and Precision Agriculture II, 6–8 November 2000, Society of Photo-Optical Instrumentation Engineers, 4203, 2000, pp. 81–90.

[36] W. Lu, J. Tan, R. Floyd, Automated fetal head detection and measurement in ultrasound images by iterative randomized Hough transform, Ultrasound Med. Biol. 31 (2005) 929–936.

[37] V. Chalana, T.C. Winter 3rd, D.R. Cyr, D.R. Haynor, Y. Kim, Automatic fetal head measurements from sonographic images, Acad. Radiol. 3 (1996) 628–635.

About the Author—WEI LU received his Ph.D. degree in the Department of Biological Engineering from the University of Missouri-Columbia in 2003. He is currently an Instructor in the Department of Radiation Oncology at Washington University in St. Louis. His research interests include image processing, pattern recognition, computer vision, and medical imaging.

About the Author—JINGLU TAN received his Ph.D. degree from the University of Minnesota in 1990. Since then, he has been on the faculty of University of Missouri, where he is currently Dowell Professor and Chair of the Biological Engineering Department. His ongoing research activities are in the areas of imaging and classification techniques for tissue differentiation, and modeling of biological processes. More information is available at http://bioengineering.missouri.edu/.